#### Research Article

Mulinti Vinodkumar Reddy, Kakanuti Malleswari, Moorthi Ajithkumar, Dalia H. Elkamchouchi, Farhan Ali, Jintu Mani Nath, Umair Khan\*, and Najiyah Safwa Khashi'ie

# Aspects of thermal radiation for the second law analysis of magnetized Darcy-Forchheimer movement of Maxwell nanomaterials with **Arrhenius energy effects**

https://doi.org/10.1515/htmp-2025-0083 received December 30, 2024; accepted June 02, 2025

Abstract: The present mathematical model investigates convective heat transfer in the Darcy-Forchheimer flow of a magneto-Maxwell nanofluid over a porous stretched sheet. The impacts of convective boundary conditions, activation energy, Joule heating, thermal radiation, and energy production are also considered in the flow model. Additionally, the heat transmission process is described using the Cattaneo-Christov heat flow model. A system of highly non-linear ordinary differential equations is built using suitable similarity transformations. The model has been numerically tackled utilizing MALAB's bvp4c package. Computational findings are calculated for liquid velocity, liquid temperature, nanoparticle concentration, and total entropy creation as functions of transverse displacement for investigating the velocity, mass, and thermal properties of the Maxwell nanoliquid under suitable assumptions and boundary conditions. Oscillations in friction factor, mass, and heat transfer rates have also been examined. It is observed that the velocity distribution improves as the thermal and concentration Grashof numbers increase, whereas it decreases as the suction parameter and Darcy–Forchheimer parameter increase. It is further reported that the concentration upsurges with larger estimates of activation energy in the central component of the geometry. This research has practical applications in escalating thermal transfer systems employed in industrial procedures, freezing technologies, and energy systems. It supports heightening thermal management in reactors, geothermal structures, and polymer processing.

Keywords: numerical simulation, Maxwell nanofluid, Darcy-Forchheimer, chemical reaction, Arrhenius energy, entropy generation

e-mail: umairkhan@sakarya.edu.tr, umair.khan@lau.edu.lb

Mulinti Vinodkumar Reddy: Department of Mathematics, Malla Reddy (MR) Deemed to be University, Medchal Malkajgiri (Dist), Hyderabad, 500100, India, e-mail: vinodmulinti15@gmail.com

**Kakanuti Malleswari:** Department of Mathematics, Malla Reddy (MR) Deemed to be University, Medchal Malkajgiri (Dist), Hyderabad, 500100, India, e-mail: malleswarik1989@gmail.com

Moorthi Ajithkumar: Department of Mathematics, Amrita School of Engineering, Amrita Vishwa Vidyapeetham, Chennai, India, e-mail: ajithkumar.research@gmail.com

Dalia H. Elkamchouchi: Department of Information Technology, College of Computer and Information Sciences, Princess Nourah bint Abdulrahman University, P.O. Box 84428, Riyadh 11671, Saudi Arabia, e-mail: dhelkamchouchi@pnu.edu.sa

Farhan Ali: Department of Mathematical Sciences, Federal Urdu University of Arts, Sciences & Technology, Gulshan-e-Iqbal Karachi, 75300, Pakistan, e-mail: farhanali@fuuast.edu.pk

Jintu Mani Nath: Department of Mathematics, Mangaldai College, Mangaldai, 784125, India, e-mail: jmnath1995@gmail.com

Najiyah Safwa Khashi'ie: Fakulti Teknologi dan Kejuruteraan Mekanikal, Universiti Teknikal Malaysia Melaka, Hang Tuah Jaya, Durian

Tunggal, Melaka, 76100, Malaysia, e-mail: najiyah@utem.edu.my

## **Nomenclature**

#### Letters

stretching rate constant р

B $\circ$ uniform magnetic field (kg  $\cdot$  S<sup>-2</sup>  $\cdot$  A<sup>-1</sup>)

Ε activation energy

Eckert number Ec

 $D_{\mathrm{B}}$ Brownian diffusion coefficient

 $D_{\mathrm{T}}$ thermophoresis diffusion coefficient

Fr Darcy-Forchheimer number

Gr thermal Grashof number

Gc concentration Grashof number

<sup>\*</sup> Corresponding author: Umair Khan, Department of Mathematics, Saveetha School of Engineering, Saveetha Institute of Medical and Technical Sciences, Saveetha University, Chennai, 602105, Tamil Nadu, India; Department of Mathematics, Faculty of Science, Sakarya University, Serdivan/Sakarya, 54050, Turkey,

 $K_{\rm r}$ rate of reaction constant K porosity parameter M magnetic field Nb Brownian motion Nt thermophoresis parameter Nu rate of heat transfer Pr Prandtl number S suction parameter Bi Biot number Sc Schmidt number Sh rate of mass transfer Т temperature of the fluid (K)  $T_{\rm w}$ temperature near the sheet (K)  $T_{\infty}$ free stream temperature (K) velocity components in x and y directions (m·s<sup>-1</sup>) u.v Cartesian coordinates (m)

## **Greek symbols**

X, y

thermal diffusivity coefficient ( $m^2 \cdot s^{-1}$ ) α В Maxwell fluid parameter chemical reaction parameter γ δ thermal relaxation parameter  $\lambda_1$ relaxation time of the heat flux similarity variable η fluid density (kg  $\cdot$  m<sup>-3</sup>) ρ  $\rho C_{\rm p}$ fluid thermal capacity ( $J \cdot m^{-3} \cdot K^{-1}$ ) kinematic viscosity ( $m^2 \cdot s^{-1}$ ) μ dynamic viscosity (kg · ms<sup>-1</sup>)

## 1 Introduction

Non-Newtonian fluids exhibit variable viscosity under stress, which has significant applications across various sectors, including biological fluid motion, food processing, rock crystal growth, microelectronic microchips, crystal fiber production, and electronic generators. The Maxwell framework is among the most significant models studied for these fluids. The Maxwell fluid is a viscoelastic material model that consists of a dashpot (a viscous component) and a spring (an elastic component) connected in series. Because it can deform like a solid and flow like a fluid, it is perfect for simulating time-dependent behavior and stress relaxation. The Maxwell fluid is frequently employed in geophysical sciences, biological mechanics, and polymer science to explain challenging material reactions to applied stress. Sara et al. [1] analyzed the mass and energy transport in Maxwell fluid over an expanding porous sheet. Amna et al. [2] investigated the Darcy-Forchheimer flow of non-Newtonian fluids through a permeable medium. Khan et al. [3] modeled the MHD irregular radiating Maxwell nanofluid in porous media, while Jawad et al. [4] explored the Darcy-Forchheimer law and hydromagnetic Maxwell fluid transport involving chemical reactions. Other researchers [5-8] have discussed non-Newtonian fluids in various contexts, further highlighting their broad implications.

Nanofluids are fluids containing nanoparticles, with particle size on a nanometer scale. These fluids are created by evenly dispersing nanoparticles in a host fluid to maintain a stable suspension, aiming to enhance thermal properties even at low concentrations. Nanofluids exhibit exceptional characteristics, making them vital to heat transfer applications. They are engineered colloidal suspensions composed of nanomaterials such as oxides, metals, carbides, or carbon nanotubes within a base liquid. Common base fluids include water, ethylene glycol, and oil. The nanoscale particles used in these fluids are typically oxides, metals, or carbides. Due to their unique properties. nanofluids are crucial in various fields, including environmental, chemical, nuclear, industrial, electrical, and medical sciences, contributing to advancements in heat management and efficiency across these domains. Buongiorno [9] explored nanoparticle mobility, including thermophoresis and Brownian movement effects. Also, it provided essential applications and models for nanomaterials. Kumar et al. [10] addressed the 2D hydromagnetic fluid of nanomaterial flow toward a stretched sheet with a chemical reaction. Mahabaleshwar et al. [11] examined the impacts of heat radiation on the flow of a Boussinesq couple stress nanofluid via a porous nonlinear stretching sheet. Saidulu and Sreeram Reddy [12] investigated the impact of dissipative heat transfer on the movement of a micropolar nanofluid across an exponentially stretched sheet. Saleem et al. [13] examined the influence of radiative energy transfer on hybrid nanomaterials across a sheet with viscous dissipation. Salahuddin et al. [14] considered the implications of activation energy for the stagnation point movement of radiative energy and heat generation with Darcy-Forchheimer. Gurejala et al. [15] investigated the magnetized Maxwell nanomaterial toward a permeable stretched sheet with a thermal source and a convective boundary condition. Mahabaleshwar et al. [16] explored the influence of radiation on the laminar movement of a dusty ternary nanofluid via a porous stretching/ shrinking sheet incorporating mass transpiration.

Activation energy is the minimum energy required by a reactive molecule to transform into a product. It represents the lowest energy needed to activate atoms or molecules for a chemical reaction or change. The concept was introduced in 1889 by the Swedish physicist Svante Arrhenius, who coined the term "activation energy." A key application of this concept lies in hyperthermia treatment, an essential component of cancer chemotherapy, where activation energy principles aid in the generation and enhancement of therapeutic effects. It is also utilized in dose measurement, which tracks the temperature range at which tumor cells are most susceptible to dying from warmth-induced death of cells during treatment with hyperthermia and counts the total quantity of thermal energy that the tumor cell has received. The activation energy of Arrhenius is most often used cumulatively in the development of medicine, stability assessment, and formulation. It probably has a significant impact on maintaining food quality. Ahmed et al. [17] explored the consequences of activation energy to study slanted upward plates in chemically reacting the Maxwell fluid flow. Bafe et al. [18] addressed the thermal bioconvection of 3D rotational movement of Williamson nanomaterials with activation energy in a Darcy-Forchheimer flow along a sheet. A study by Ali et al. [19] examined the Darcy-Forchheimer nanofluid circulation over a vertical plate that included a permeable medium and radiation. The Darcy-Forchheimer motion of Maxwell tiny fluids across a permeable stretched surface with buoyancy forces and Arrhenius energy was examined by Jawad et al. [20]. The passage of Prandtl nanofluids and heat radiation via a porous extended surface contained in a Darcy-Forchheimer media was examined by Zafar et al. [21]. Li et al. [22] discussed the impact of Darcy law on a micropolar fluid flow across a channel.

Ghazwani et al. [23] studied the energy and fluid motion within the framework of non-radiative conditions and Cattaneo-Christov energy flux across a slanted extended cylinder. Yasir et al. [24] explored the influence of mass transfer on Maxwell fluid flow along a stretched cylinder using the innovative Cattaneo-Christov thermal transport model. Jabeen et al. [25] investigated mass and energy characteristics in Maxwell fluid motion, incorporating Cattaneo-Christov fluxes under linear stretching conditions. The Cattaneo-Christov model in magnetized Maxwell fluid across a permeable stretched surface with thermal generation was examined by Jawad and Nisar [26]. Awais et al. [27] addressed the entropy generation process in Darcy-Forchheimer flow, considering the effects of viscous dissipation, variable fluid properties, and activation energy. Khan et al. [28] analyzed the entropy in the hydrodynamic transport of non-Newtonian fluids, accounting for viscous dissipation and Arrhenius activation energy. Hamid and Khan [29] examined the magneto-Williamson nanofluid flow over a circular cylinder,

incorporating the effects of activation energy. Zeeshan et al. [30] focused on entropy generation in non-Newtonian fluid flow past a stretched cylinder. Sharma et al. [31] investigated entropy analysis in the electro-magnetohydrodynamic flow of Jeffrey fluid, including the effects of radiation and magnetohydrodynamics.

In light of the aforementioned significant research openings, the present effort investigates the impact of the convectional heat transfer effect on the Darcy-Forchheimer movement of a Maxwell nanofluid across a porous stretched surface in the presence of hydrodynamics. Important components, including heat radiation, energy creation, and viscous dissipation, are taken into consideration in the mathematical model. The study investigates the flow and thermal characteristics of Maxwell nanoliquid across a porous stretched sheet under the influence of relevant physical factors by applying numerical simulations using MATLAB's bvp4c tool. The discoveries demonstrate that when the thermal and concentration Grashof numbers grow, the distribution of velocity gets stronger, whereas it decreases as the suction parameter and Darcy-Forchheimer factor increase. The study reports that the concentration increases with higher activation energy estimates in the core region of the geometry.

The novelty of this research lies in investigating Maxwell nanofluid movement over a porous stretched surface by integrating convectional thermal transport, Darcy-Forchheimer impacts, radiation, and viscous dissipation, offering an inclusive and accurate model of intricate thermal-fluid behavior. This investigation has practical applications in elevating thermal transfer systems used in industrial procedures, freezing technologies, and energy systems. It supports optimizing heat management in reactors, geothermal structures, and polymer processing.

## 2 Mathematical modeling

This work examines the entropy analysis in Darcy-Forchheimer motion of magneto-Maxwell nanomaterial over a porous stretching surface, considering the effects of radiative heat transfer, activation energy, Joule heating, energy generation, and convective boundary conditions. Further, the heat transmission process is described using the Cattaneo-Christov thermal flow concept. The movement of nanoparticle effects is witnessed with the help of Buongiorno's model. In the analysis, the y-axis is considered to be perpendicular to the extended sheet, which has a velocity u along the x-axis. In Figure 1, the flow phenomena and the magnetic field intensity  $B_0$  positioned perpendicular to it are depicted. In the

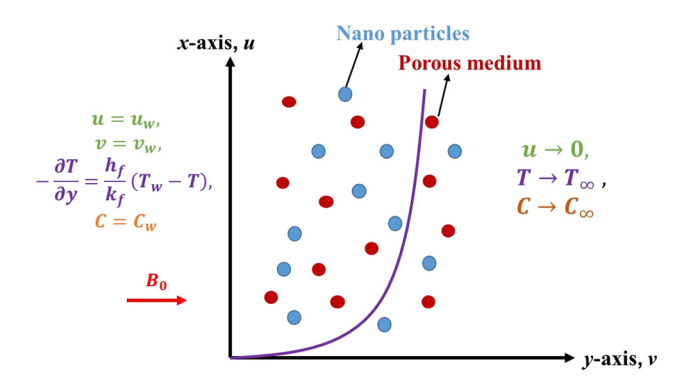


Figure 1: Pictorial demonstration of the flow model.

suggested Maxwell nanofluid flow model, the proper set of partial differential equations is written in the following manner [15,26]:

$$\frac{\partial u}{\partial x} + \frac{\partial v}{\partial y} = 0,\tag{1}$$

$$u\frac{\partial u}{\partial x} + v\frac{\partial u}{\partial y} = \vartheta \frac{\partial^{2} u}{\partial y^{2}} - \lambda_{1} \left[ u^{2} \frac{\partial^{2} u}{\partial x^{2}} + v^{2} \frac{\partial^{2} u}{\partial y^{2}} + 2uv \frac{\partial^{2} u}{\partial x \partial y} \right]$$

$$- \frac{\sigma B_{0}^{2} u}{\rho} - \frac{\mu}{\rho k_{1}} u - \frac{c_{b}}{\sqrt{k_{1}}} u^{2}$$

$$+ g\beta_{T} (T - T_{\infty}) + g\beta_{C} (C - C_{\infty}),$$

$$(2)$$

$$u\frac{\partial T}{\partial x} + v\frac{\partial T}{\partial y} = \left(\frac{k}{\rho C_{P}}\right)\frac{\partial^{2} T}{\partial y^{2}} + \left(\frac{\mu}{\rho C_{P}}\right)\left(\frac{\partial u}{\partial y}\right)^{2}$$

$$+ \tau \left(D_{B}\frac{\partial C}{\partial y}\frac{\partial T}{\partial y} + \frac{D_{T}}{T_{\infty}}\left(\frac{\partial T}{\partial y}\right)^{2}\right) - \frac{1}{\rho C_{P}}\frac{\partial q_{T}}{\partial y}$$

$$- \lambda_{2}\left[u\frac{\partial T}{\partial x}\frac{\partial u}{\partial x} + v\frac{\partial T}{\partial y}\frac{\partial v}{\partial y} + u\frac{\partial T}{\partial y}\frac{\partial v}{\partial x} + v\frac{\partial u}{\partial y}\frac{\partial T}{\partial x} + 2uv\frac{\partial^{2} T}{\partial x\partial y} + u^{2}\frac{\partial^{2} T}{\partial x^{2}} \right]$$

$$+ v^{2}\frac{\partial^{2} T}{\partial y^{2}} + \frac{1}{\rho C_{P}}\left[\mu_{f}\left(\frac{\partial u}{\partial y}\right)^{2} - \lambda_{1}\left[v^{2}\left(\frac{\partial u}{\partial y}\right)^{2} + 2uv\frac{\partial u}{\partial x}\frac{\partial u}{\partial y}\right]\right]$$

$$+ \frac{Q_{0}}{\rho C_{P}}(T - T_{\infty}) + \frac{\sigma B_{0}^{2}}{\rho C_{P}}u^{2},$$

$$u\frac{\partial C}{\partial x} + v\frac{\partial C}{\partial y} = D_{B}\frac{\partial^{2} C}{\partial y^{2}} + \frac{D_{T}}{T_{\infty}}\frac{\partial^{2} T}{\partial y^{2}}$$

$$- K_{T}^{2}(C - C_{\infty})\left(\frac{T}{T}\right)^{n} \exp\left(\frac{-E_{a}}{kT}\right).$$
(4)

The considered boundary conditions are as follows:

$$u = u_{w}, \quad v = v_{w}, \quad C = C_{w},$$

$$\frac{\partial T}{\partial y} = \frac{-h_{f}}{k_{f}} (T_{w} - T) \quad \text{at} \quad y = 0$$

$$u \to 0, \quad C \to C_{\infty}, T \to T_{\infty} \quad \text{as} \quad y \to \infty.$$
(5)

Introducing the similarity transformations

$$u = pxf'(\eta), \quad v = -(p\vartheta)^{\frac{1}{2}} \quad f(\eta),$$

$$N = px\sqrt{\frac{p}{\vartheta}}, \eta = \sqrt{\frac{p}{\vartheta}} \quad y,$$
(6)

$$T-T_{\infty}=\theta(\eta)(T_{\mathrm{W}}-T_{\infty}), C-C_{\infty}=\varphi(\eta)(C_{\mathrm{W}}-C_{\infty}).$$

The subsequent dimensionless equations were obtained through application of the similarity transforms found in equations (2)–(5) as follows:

$$f''' + ff'' + \beta(2ff'f'' - f^2f''') - (M + K)f' + Gr\theta + Gc\phi - Frf'^2 - f'^2 = 0,$$
(7)

$$((1+R) - \Pr\delta f^2)\theta'' + \Pr[f\theta' - \delta f f'\theta' + \text{Nb}\theta'\phi' + \text{Nt}\theta'^2 + M\text{Ec}f'^2]$$

$$+ \beta(2f f'^2 f'' - f^2 f''^2) + \PrO\theta + \Pr \text{Ec}f''^2 = 0,$$
(8)

$$\varphi'' + \operatorname{Sc} f \varphi' + \frac{\operatorname{Nt}}{\operatorname{Nb}} \theta'' - \operatorname{Sc} \gamma (1 + \alpha_1 \theta)^n \exp\left[\frac{-E}{1 + \alpha_1 \theta}\right] \varphi = 0. \quad (9)$$

The corresponding boundary conditions are as follows:

$$f(0) = S, \quad f'(0) = 1, \ \varphi(0) = 1,$$
  

$$\theta'(0) = -Bi(1 - \theta(0))$$
  

$$f'(\infty) = 0, \ \varphi(\infty) = 0, \ \theta(\infty) = 0.$$
(10)

where

$$M = \frac{\sigma B_{\circ}^{2}}{\rho p}, \quad K = \frac{\upsilon}{pk_{1}}, \quad F_{r} = \frac{c_{b}}{\sqrt{k_{1}}},$$

$$Gc = \frac{(C_{W} - C_{\infty})gx\beta_{C}}{u_{w}^{2}}, \quad Gr = \frac{g(T_{W} - T_{\infty})\beta_{T}x}{u_{w}^{2}},$$

$$\delta = p\lambda_{2}, \quad R = \frac{16\sigma^{*}T_{\infty}^{3}}{3k^{*}k}, \quad Pr = \frac{\upsilon}{\alpha}, \quad Q = \frac{Q_{\circ}}{\rho C_{p}p},$$

$$Ec = \frac{u_{w}^{2}}{(T_{W} - T_{\infty})C_{p}},$$

$$Nb = \frac{\tau D_{B}(C_{W} - C_{\infty})}{\upsilon}, \quad Nt = \frac{\tau D_{T}(T_{W} - T_{\infty})}{T_{\infty}\upsilon},$$

$$Sc = \frac{\upsilon}{D_{B}}, \quad \gamma = \frac{K_{r}^{2}}{p}, \quad E = \frac{E_{a}}{kT_{\infty}},$$

$$S = -\frac{\upsilon_{W}}{\sqrt{p\upsilon}}, \quad Bi = \frac{h_{f}}{k}\sqrt{\frac{\upsilon}{p}}.$$

$$(11)$$

The rates of mass, heat, and skin friction are defined as follows:

$$\frac{\mathrm{Sh}}{\sqrt{\mathrm{Re}_x}} = -\varphi'(0), \quad \frac{\mathrm{Nu}}{\sqrt{\mathrm{Re}_x}} = -(1+R)\theta'(0),$$

$$\sqrt{\mathrm{Re}_x} C_f = f''(0),$$
(12)

where  $Re_x = \frac{px^2}{v}$  is the local Reynolds number.

## 3 Examination of entropy generation

The following is the mathematical representation of the Maxwell fluid's volumetric entropy:

$$S_{G} = \frac{k}{T_{\infty}^{2}} \left[ 1 + \frac{16\sigma^{*}T_{\infty}^{3}}{3k^{*}k} \right] \left( \frac{\partial T}{\partial y} \right)^{2} + \frac{\sigma B_{0}^{2}}{T_{\infty}} u^{2} + \frac{RD}{C_{\infty}} \left( \frac{\partial C}{\partial y} \right)^{2} + \frac{RD}{T_{\infty}} \left( \left( \frac{\partial C}{\partial y} \right) \left( \frac{\partial T}{\partial y} \right) \right) + \frac{\mu_{f}}{k_{1}T_{\infty}} u^{2} + \frac{1}{T_{\infty}} \left[ -\lambda_{1} \left( \left( \frac{\partial u}{\partial y} \right)^{2} v^{2} + 2uv \frac{\partial u}{\partial x} \frac{\partial u}{\partial y} \right) + \mu_{f} \left( \frac{\partial u}{\partial y} \right)^{2} \right].$$

$$(13)$$

Substituting equation (6) in equation (13), we obtain

Ns = 
$$\alpha_1 (1 + R)\theta'^2 + \text{Br}(f''^2 + \beta(2ff'^2f'' - f^2f''^2))$$
  
+  $L\left[\frac{\alpha_2}{\alpha_1}\right]\varphi'^2 + \text{Br}(M + K)f'^2 + L\theta'\varphi',$  (14)

where

$$L = \frac{D(C_{\rm w} - C_{\infty})R}{k}, \text{ Br} = \frac{\mu_f u_{\rm w}^2}{\Lambda T k}, \quad \alpha_2 = \frac{\Delta C}{C_{\infty}}, \quad \alpha_1 = \frac{\Delta T}{T_{\infty}} \quad (15)$$

are the diffusion parameter, Brinkman number, concentration, and thermal difference parameters, respectively.

## Methodology

Let us introduce the variables  $f_1 = f$ ,  $f_2 = f'$ ,  $f_3 = f''$ ,  $f_4$  =  $\theta$  ,  $f_5$  =  $\theta^{'}f_6$  =  $\varphi$  ,  $f_7$  =  $\varphi^{'}$ . Now, the governing equations and the boundary conditions can be written as follows:

$$f_1' = f(2),$$
 (16)

$$f_2' = f(3),$$
 (17)

$$f_3' = \frac{1}{(1 - \beta f_1^2)} ((M + K)f_2 - f_1 f_3 - 2\beta f_1 \quad f_2 \quad f_3 - Gr f_4 - Gc f_6 + Fr f_2^2 + f_2^2),$$
(18)

$$f_{4}^{\prime}=f(5), \tag{19}$$

$$f_5' = \frac{1}{[(1+R) - \Pr{\delta f_1 f_1}]} (\Pr{\delta f_1 f_2 f_5} - f_1 f_5 - \text{Nb} f_5 f_7 - \text{Nt} f_5 f_5 - M \text{Ec} f_2 f_2 + \beta (2f_1 f_2^2 f_3 - f_1^2 f_3^2) - Q f_4$$

$$- \text{Ec} f_3 f_3),$$
(20)

$$f_{\mathcal{E}}' = f(7), \tag{21}$$

$$f_{7}' = -\frac{\text{Nt}}{\text{Nb}} \left[ \frac{1}{[(1+R) - \text{Pr}\delta f_{1}f_{1}]} (\text{Pr}[\delta f_{1}f_{2}f_{5} - f_{1}f_{5} - \text{Nb}f_{5}f_{7} - \text{Nt}f_{5}f_{5} - M\text{Ec}f_{2}f_{2} + \beta(2f_{1}f_{2}^{2}f_{3} - f_{1}^{2}f_{3}^{2}) - Qf_{4} - \text{Ec}f_{3}f_{3}]) \right] + \text{Sc}\gamma(1 + \alpha_{1}f_{4})^{n} \exp\left[\frac{-E}{1 + \alpha_{1}f_{4}}\right] f_{6}$$

$$- \text{Sc}f_{1}f_{7}. \tag{22}$$

With the boundary conditions:

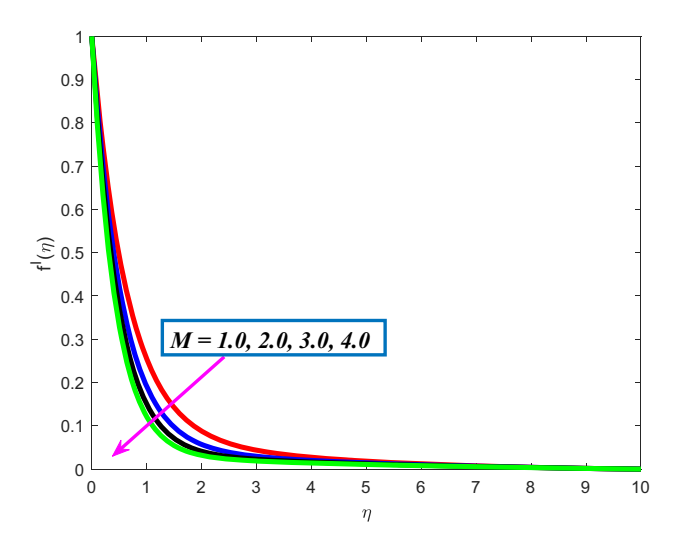
$$f_1 = S, f_2 = 1, f_5 = -\text{Bi}(1 - f_4), f_6 = 1$$
  
at  $\eta = 0, f_2 = 0, f_4 = 0, f_6 = 0$  as  $\eta \to \infty$ . (23)

The numerical solutions for the above equations are obtained by the Runge-Kutta method with a shooting technique and implemented via the BVP4C MATLAB package.

## 5 Results and discussion

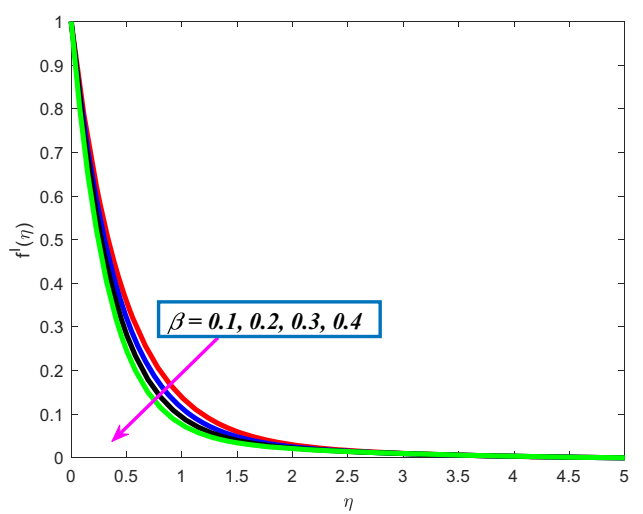
In this section, the numerical calculation for the nonlinear ODEs (7), (8), and (9) with the pertinent boundary circumstances (10) is thoroughly scrutinized. In order to resolve the fluid flow equation computationally, the fourth-order Runge-Kutta method and the well-known shooting method are combined. Additionally, using the specified boundary conditions, graphs and tabular representations of the numerical results of the current flow problem have been made possible by MATLAB's byp4c solver. For this analysis each parameter is numerically computed by assigning fixed values to other associated parameters such as M =0.5, K = 0.1, Fr = 0.3, Bi = 0.3, Nb = 0.2, Nt = 0.2, Sc = 0.5, Q = 0.50.2,  $\gamma = 0.5$ , Pr = 0.72, R = 0.5, Br = 0.5,  $\beta = 0.1$ , E = 0.5, Lb = 1, Pe = 0.15,  $\delta_1$  = 0.2,  $\alpha_1$  = 0.3,  $\alpha_2$  = 0.2, and S = 0.1.

The effect of the magnetic factor (M) on the outline of velocity  $(f'(\eta))$  is demonstrated in Figure 2. The ascending levels of M show the velocity curve's declining behavior. Since M is the ratio of Lorentz forces to viscosity forces, physically speaking, an increase in the magnetic field strengthens the Lorentz force and decreases the fluid's velocity. The effect of the magnetic component (M) on the thermal field  $(\theta(\eta))$  is described by Figure 3. It reveals the increasing profile of thermal distribution  $\theta(\eta)$  due to



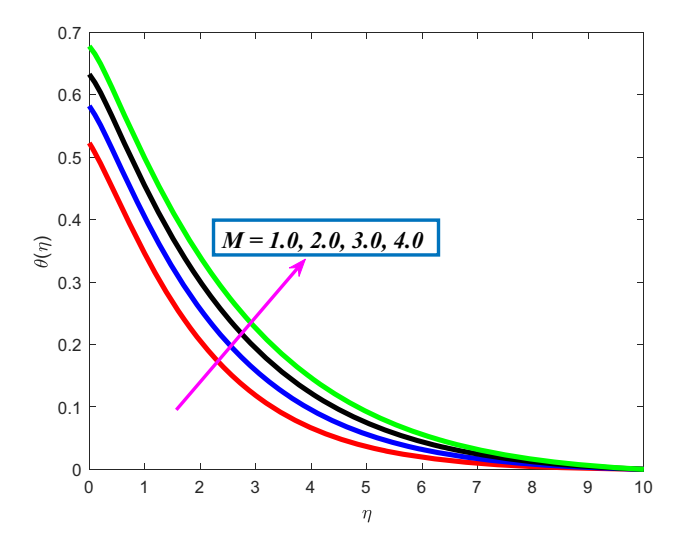
**Figure 2:**  $f'(\eta)$  for various M values.

the dominant magnetic parameter. Figure 4 describes the outputs of the velocity region  $(f'(\eta))$  for larger values of Maxwell parameter, denoted as  $\beta$ . It is noted that the liquid speed and the overall thickness of the mobility boundary layer diminished as we increased Maxwell parameter quantities. Increasing the Maxwell factor physically causes viscoelastic effects to appear in the fluid movement, resulting in greater friction within the system and creating a barrier. Due to its viscoelastic properties, the formation of molecular groupings restricts the free movement of the fluid, resulting in a reduction in its speed. Figure 5 depicts the effect of the porous factor (K) on the velocity  $(f'(\eta))$ . It was observed that when the values of the porosity component increase, the velocity distribution falls. In physical terms, boosting the porosity parameter lowers the speed

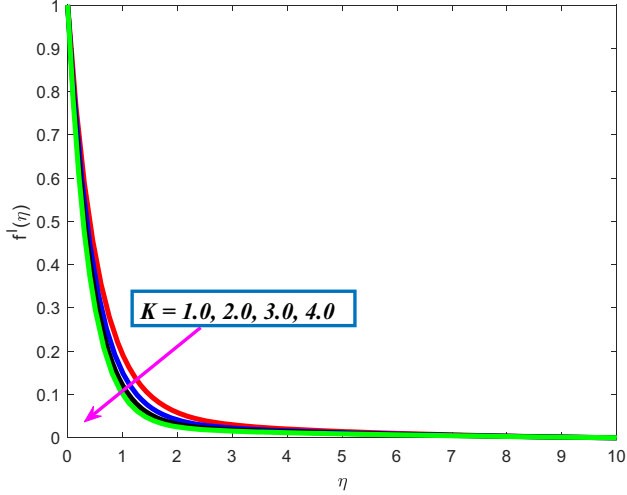


**Figure 4:**  $f'(\eta)$  for various  $\beta$  values.

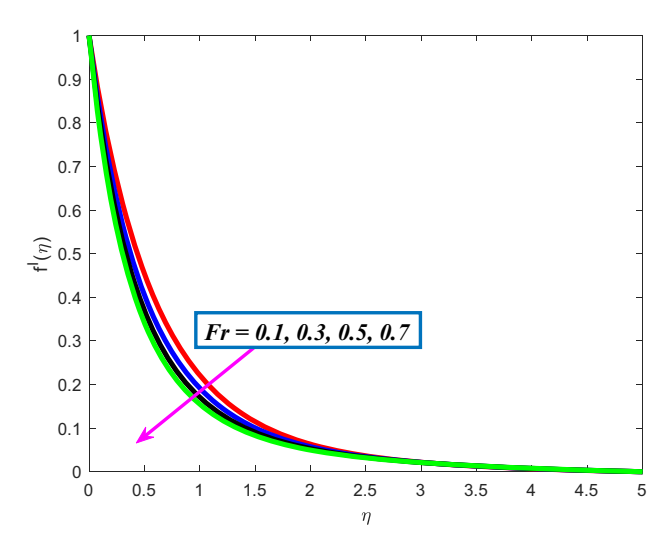
because the fluid flow is resisted by the medium's porosity, which leads to obstructions and higher friction. Figure 6 shows how  $f'(\eta)$  varies as the Forchheimer number Fr increases. Physically, a porous material is one kind of opposing factor that seeks to impede the flow of a liquid flowing across it, hence reducing the flow's speed. Figure 7 depicts the behavior of velocity for various values of thermal Grashof number (Gr). It is noted that the increase in velocity is higher for the higher values of Gr. Figure 8 demonstrates the effect of concentration Grashof number (Gc) on the velocity profile. It provides that the increased Gc declines the velocity. Figure 9 draws attention to the thermal distribution  $\theta(\eta)$  for greater temperature relaxation factor  $(\delta)$ . It is demonstrated that the energy field diminishes as  $\delta$  is increased. Figure 10 reveals the impact



**Figure 3:**  $\theta(\eta)$  for various M values.

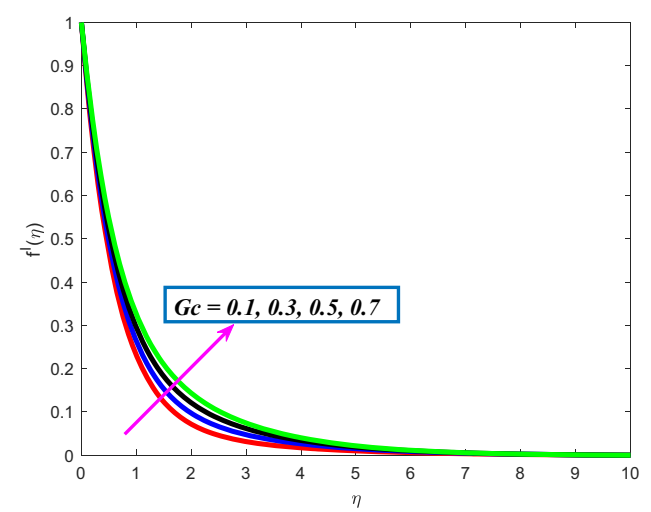


**Figure 5:**  $f'(\eta)$  for various K values.



**Figure 6:**  $f'(\eta)$  for various Fr values.

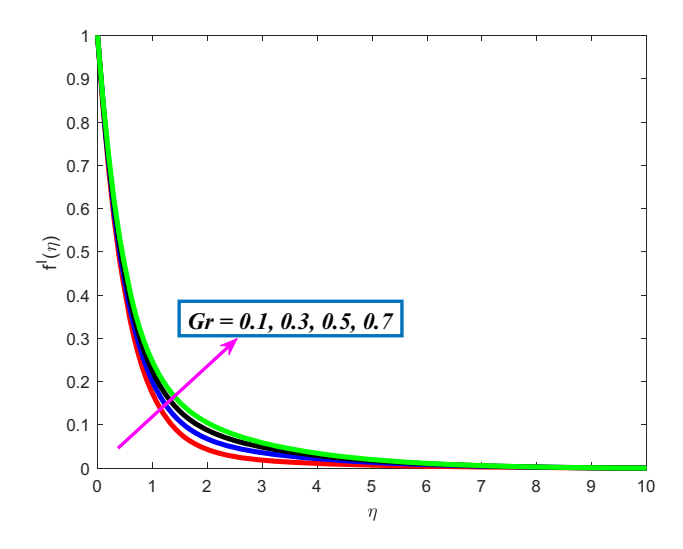
of the radiation parameter (R) on the thermal field  $(\theta(\eta))$ . It is noticed that  $\theta$  is enhanced with a strengthened amount of R. In reality, additional energy is created inside the liquid due to a boost in the parameter for radiation (R), which therefore improves the energy profile. Figures 11 and 12 depict the behavior of mass and thermal profiles for disparate values of the Brownian motion parameter (Nb). The parameter Nb tends to increase the temperature and reduce the concentration. Brownian motion refers to the random and unpredictable movement of particles in a liquid due to frequent collisions with fast-moving molecules. These collisions generate heat, leading to a rise in temperature. Similarly, the concentration of species among nanoparticles decreases as repeated collisions



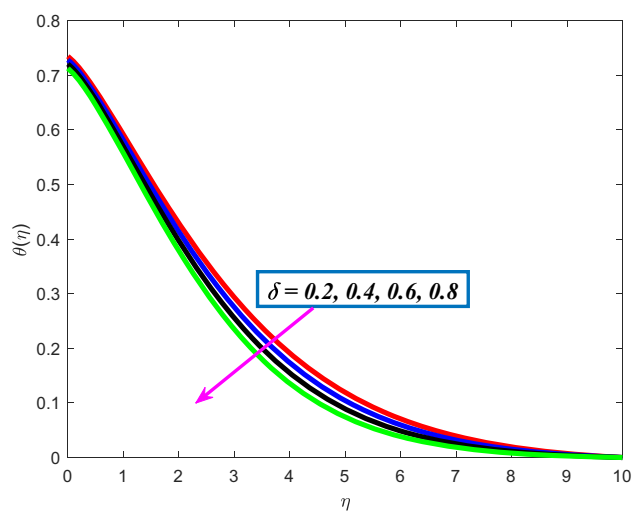
**Figure 8:**  $f'(\eta)$  for various Gc values.

cause dispersion, highlighting the dynamic interaction between particles and their surroundings.

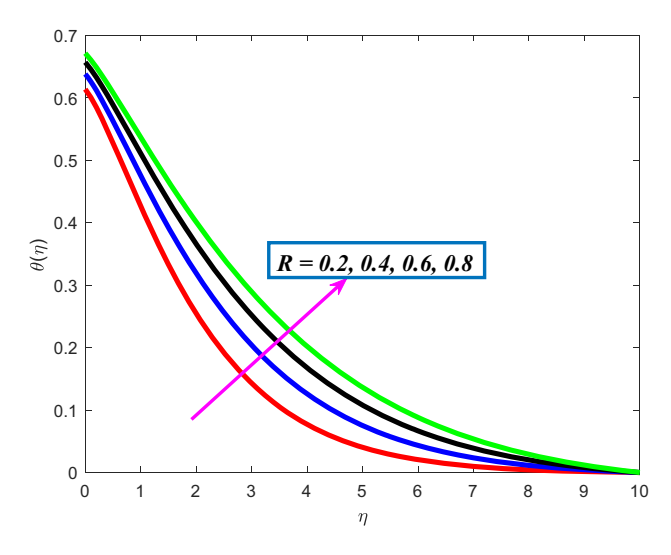
Figure 13 shows the changes in the solutal field with the thermophoresis parameter (Nt). The behavior of concentration distribution is increased with strengthened Nt. Figure 14 elaborates the concentration field  $\varphi(\eta)$  for a wide range of values in activation energy (E). The concentration profile improves as a result of the supplementing values of E. Figure 15 presents a sketch for the concentration profile  $\varphi(\eta)$  against different values of Schmidt number (Sc). Generally, the dominating Sc diminishes the mass diffusion coefficient, which reduces the concentration field. Figure 16 reveals how the concentration field is affected by the chemical reaction parameter  $(\gamma)$ . It is found that the concentration field is reduced by raising chemical reactions.



**Figure 7:**  $f'(\eta)$  for various Gr values.

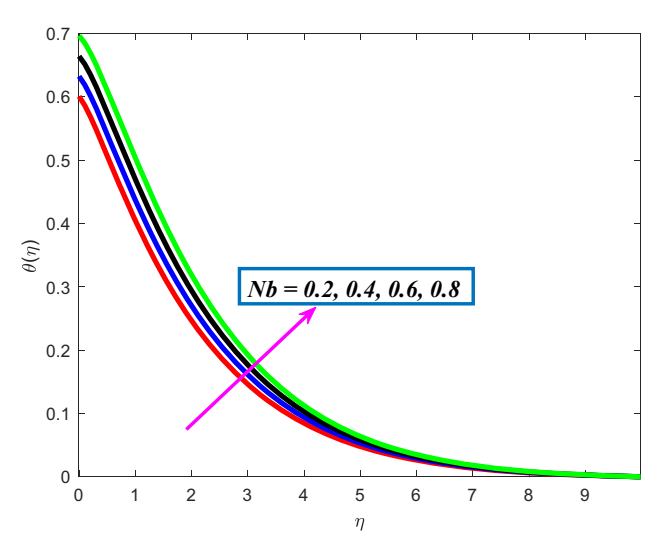


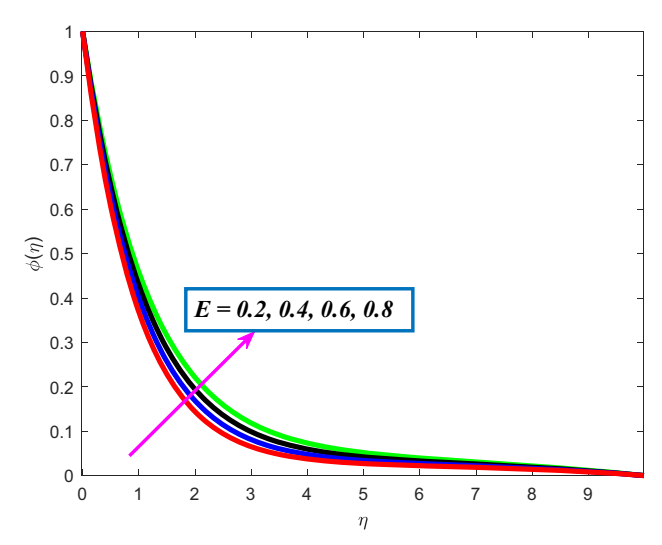
**Figure 9:**  $\theta(\eta)$  for various  $\delta$  values.



**Figure 10:**  $\theta(\eta)$  for various R values.

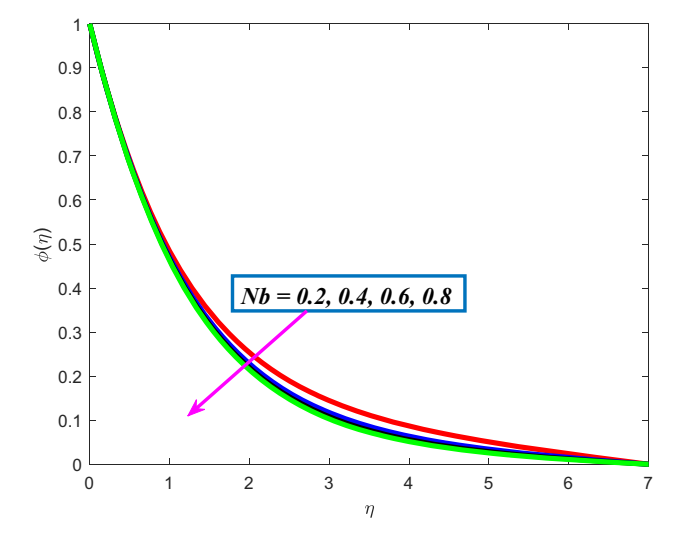
**Figure 13:**  $\varphi(\eta)$  for various Nt values.





**Figure 11:**  $\theta(\eta)$  for various Nb values.

**Figure 14:**  $\varphi(\eta)$  for various E values.



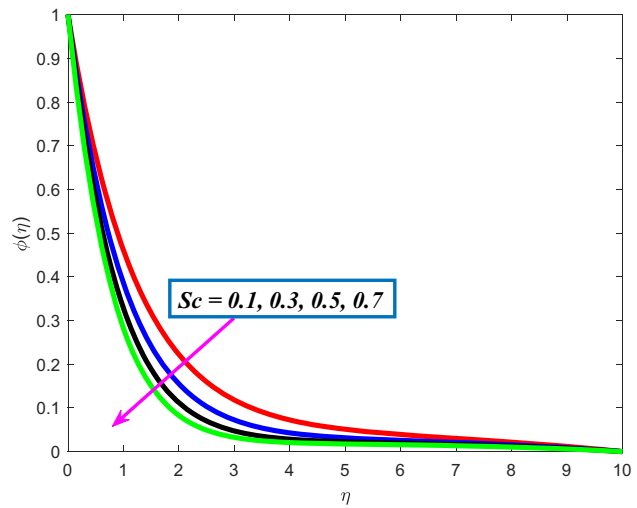
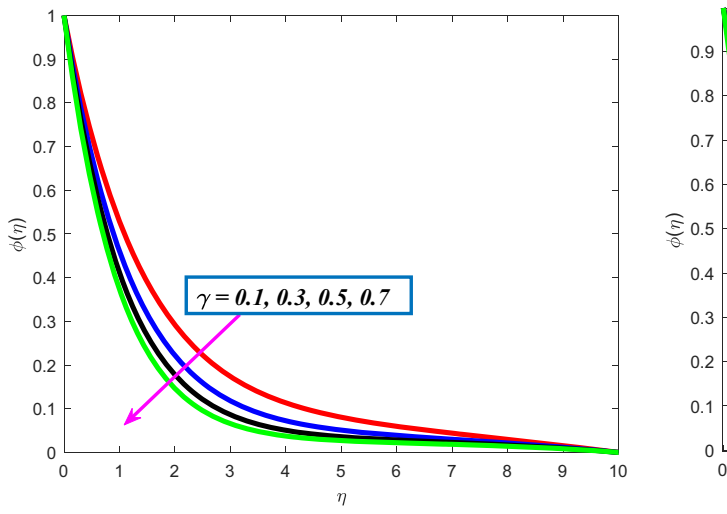


**Figure 12:**  $\varphi(\eta)$  for various Nb values.

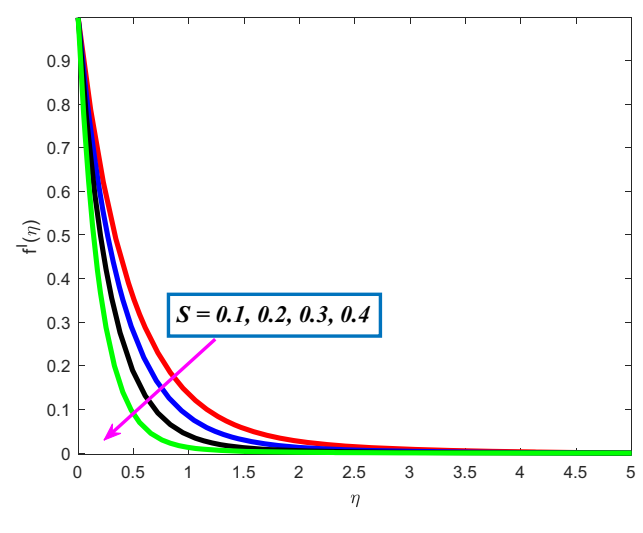
**Figure 15:**  $\varphi(\eta)$  for various Sc values.

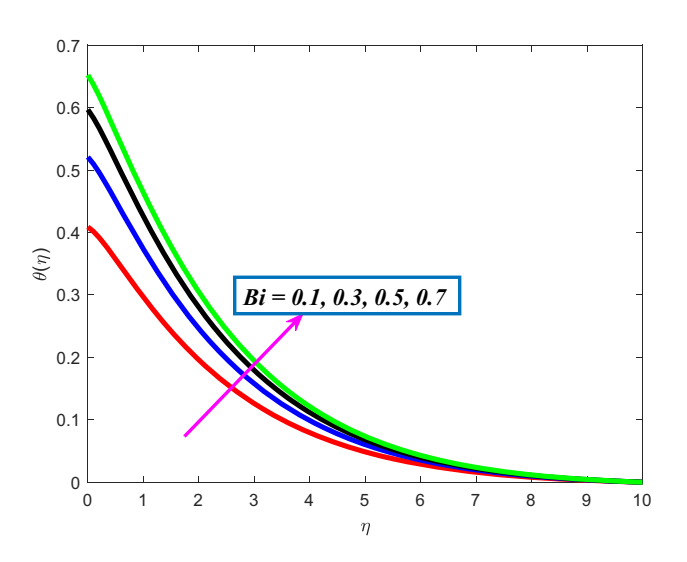


S = 0.1, 0.2, 0.3, 0.40.5 4.5

**Figure 16:**  $\varphi(\eta)$  for various  $\gamma$  values.

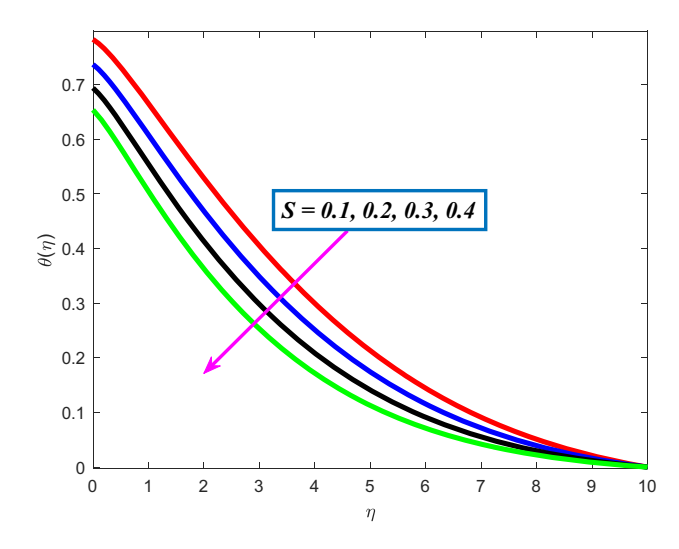
**Figure 19:**  $\varphi(\eta)$  for various *S* values.





**Figure 17:**  $f'(\eta)$  for various S values.

**Figure 20:**  $\theta(\eta)$  for various Bi values.



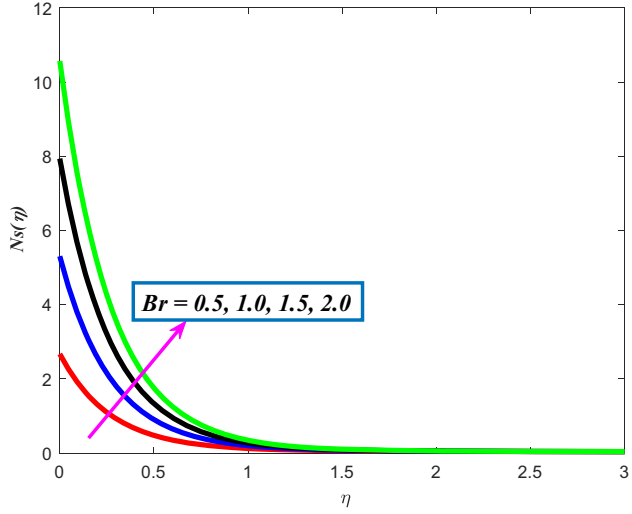


**Figure 18:**  $\theta(\eta)$  for various S values.

**Figure 21:**  $Ns(\eta)$  for various Br values.

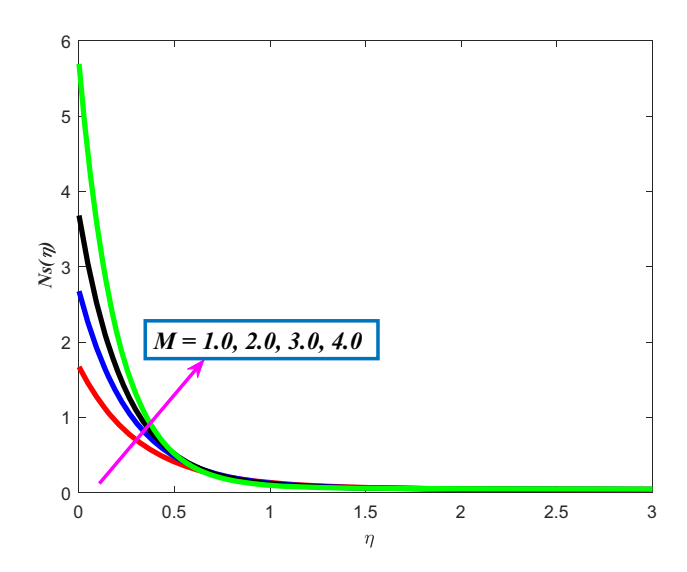


**Figure 22:**  $Ns(\eta)$  for various M values.

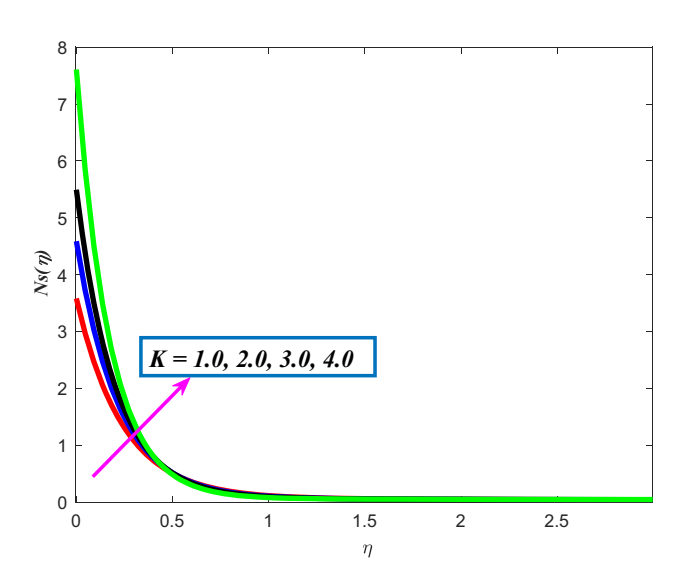


**Figure 23:**  $Ns(\eta)$  for various K values.

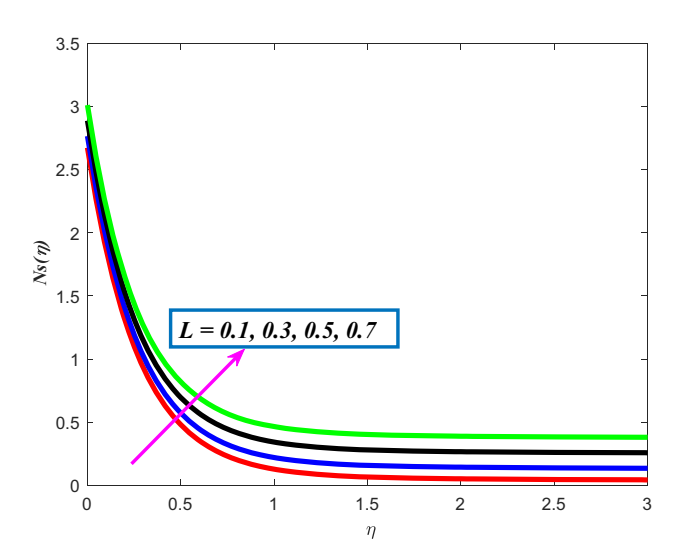


**Figure 24:**  $Ns(\eta)$  for various L values.

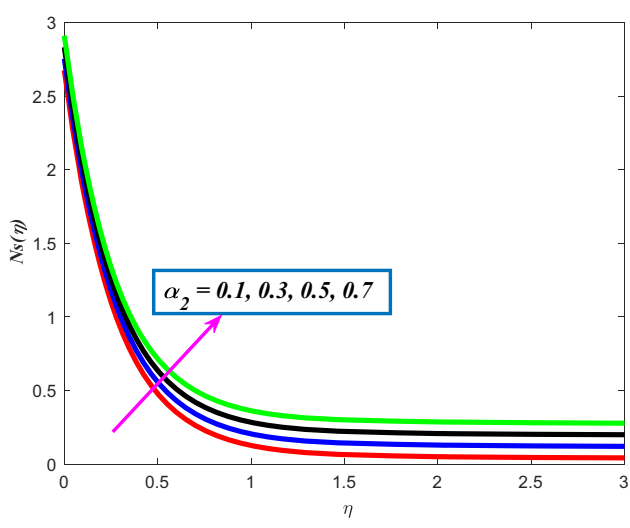


**Figure 25:** Ns( $\eta$ ) for various  $\alpha_2$  values.

Figures 17-19 illustrate the consequence of the suction factor (S) on the liquid velocity  $(f'(\eta))$ , thermal profile  $(\theta(\eta))$ , and solute profile  $(\varphi(\eta))$ . The thermal, velocity, concentration, and the corresponding boundary layer thickness profiles show a drop over the whole boundary layer area for higher values of the suction parameter. In physical terms, a higher suction parameter results in a greater amount of fluid being removed, which reduces the fluid's velocity at the surface and slows down the flow. Figure 20 shows the Biot number (Bi) effects on the thermal field  $(\theta(\eta))$ . It is noticed that the increment in Bi improves the temperature. Figures 21-26 depict the entropy generation  $(Ns(\eta))$  under the effects of Brinkman number (Br), magnetic field parameter (M), porosity parameter (K), diffusion parameter (L), concentration difference parameter  $(\alpha_2)$ , and radiation (R). It is found that the Ns $(\eta)$  enhanced with enhancement in Br, M, K, L,  $\alpha_2$ , and R.

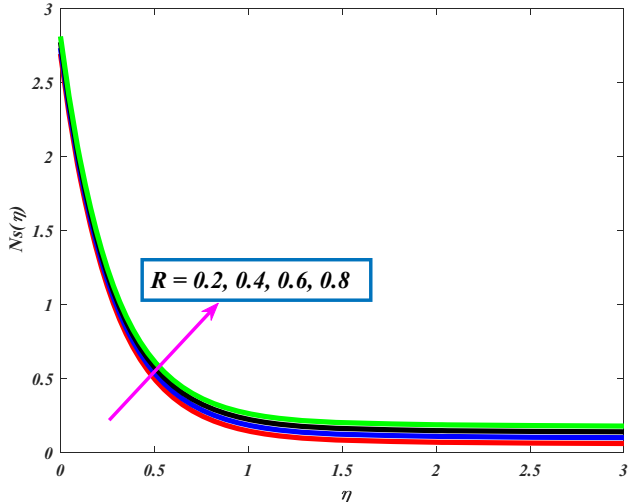


**Figure 26:**  $Ns(\eta)$  for various R values.

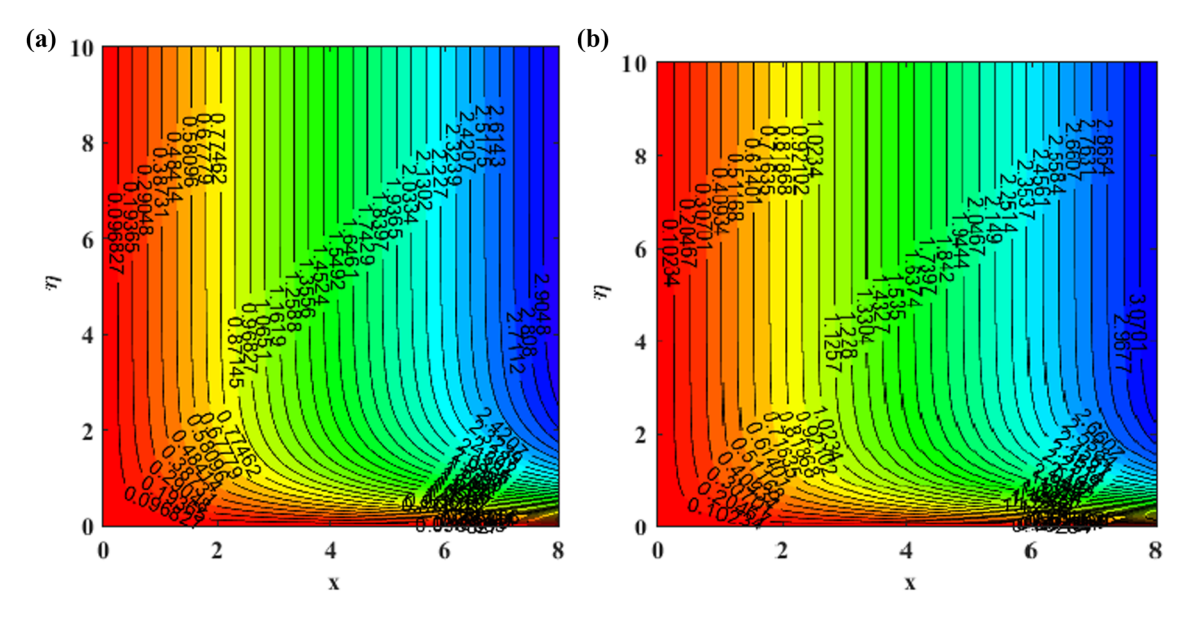


Figure 27: (a and b) Streamlines profile.

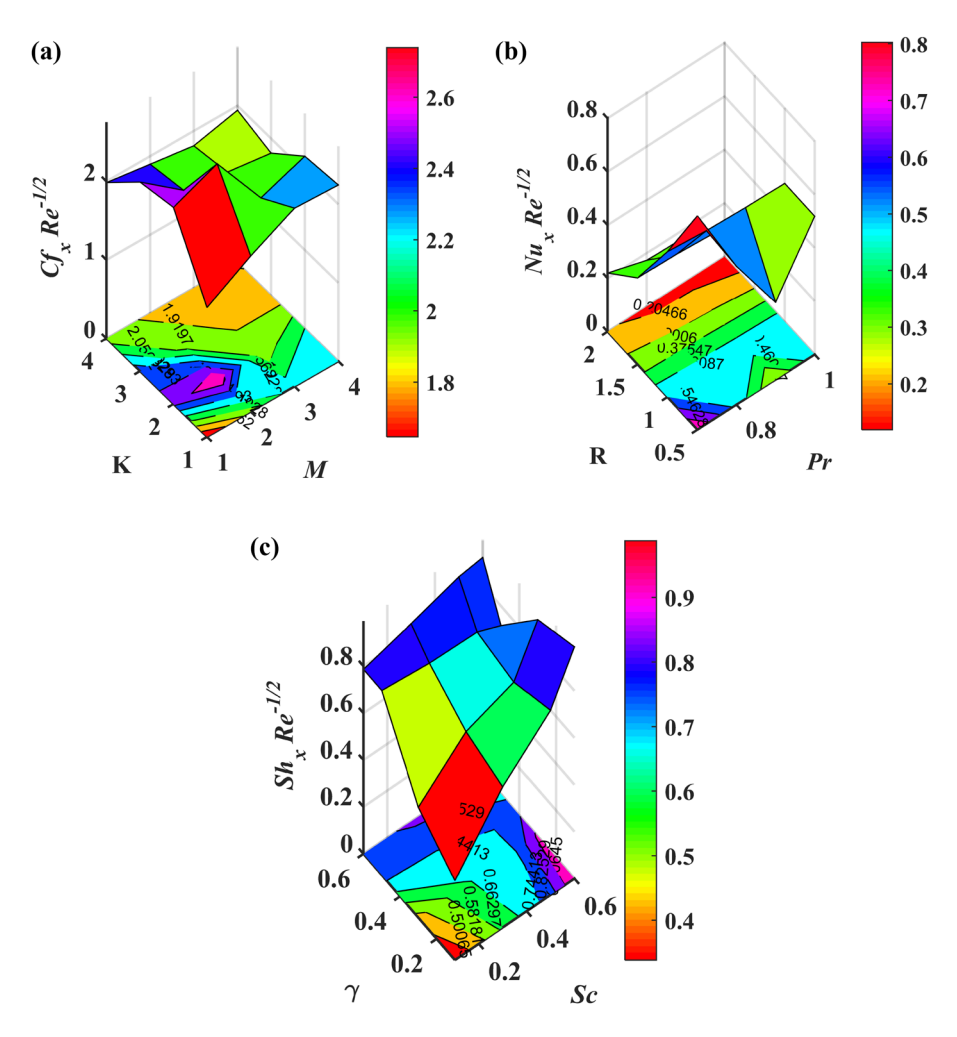


Figure 28: (a)–(c) Surface plot of skin friction coefficient, Nusselt number and Sherwood number.

**Table 1:** Variations in skin friction for various parameters

M	K	β	Gr	Gc	Fr	S	$C_{\rm f}({\rm Re}_x)^{\frac{1}{2}}$
1.0							-1.646613
2.0							-1.983847
3.0							-2.271701
	1.0						-2.245651
	2.0						-2.504542
	3.0						-2.738965
		0.1					-1.983847
		0.2					-2.193957
		0.3					-2.409157
			0.1				-1.983847
			0.3				-1.894008
			0.5				-1.814466
				0.1			-1.983847
				0.3			-1.897335
				0.5			-1.810797
					0.1		-1.942817
					0.3		-1.983847
					0.5		-2.024084
						0.1	-1.983847
						0.2	-2.057192
						0.3	-2.135494

Contour plots are examined for different values of M and K, as shown in Figure 27(a) and (b). Figure 28(a)—(c) shows a sketch to view the skin friction, heat, and mass transmission rate against M, K, R, Pr, Sc, and  $\gamma$ . Figure 28(a) shows that the skin friction diminishes with an elevation in the M and K due to the inverse connection between them, as the ratio of inertia to viscous forces increases. Moreover, higher values of M and K cause an escalation in friction forces, thus leading to an increase in skin friction. The effect of Pr and R on heat transfer is shown in Figure 28(b). It is clear that higher Pr and R result in a greater Nusselt number, which in turn causes a higher temperature profile, and so on. Furthermore, increases in the Sc and  $\gamma$  increase in the Sherwood number.

Table 1 depicts that the friction factor declines with enhancement in  $M, K, \operatorname{Fr}, \beta$ , and S, while opposite behavior is seen with enhancement in Gr and Gc. Table 2 presents the heat transfer rate increases for increasing values of M, Q, Ec, Nb, and Nt, but a reverse phenomenon is observed in the case of Pr, and Bi. Table 3 depicts that the larger values of Sc,  $\gamma$ , Nt, and E enhance the mass transfer rate. Moreover, Table 4 is constructed to present the individuality of this study.

**Table 2:** Deviations in the rate of mass transmission for various parameters

M	Pr	R	Q	Ec	Nb	Nt	δ	Bi	$(Re_x)^{-\frac{1}{2}}Nu$
1.0									0.080249
2.0									0.051925
3.0									0.028946
	0.7								0.051863
	8.0								0.052540
	0.9								0.054044
		0.5							0.055279
		1.0							0.051925
		1.5							0.052367
			0.1						0.051925
			0.2						-0.107686
			0.3						-0.694490
				0.1					0.051925
				0.2					0.017309
				0.3					-0.016940
					0.2				0.051925
					0.4				0.046719
					0.6				0.041765
						0.2			0.051925
						0.4			0.048915
						0.6			0.045768
							0.2		0.051925
							0.4		0.045171
							0.6		0.041477
								0.1	0.031962
								0.3	0.051925
								0.5	0.059454

**Table 3:** Variations in the rate of mass transmission for various parameters

Sc	γ	Nb	Nt	E	$(Re_x)^{-\frac{1}{2}}Sh$
0.1					0.338323
0.3					0.600189
0.5					0.786415
	0.1				0.470914
	0.3				0.654791
	0.5				0.786415
		0.2			0.786415
		0.4			0.765138
		0.6			0.758990
			0.2		0.786415
			0.4		0.842619
			0.6		0.903393
				0.2	0.786415
				0.4	0.848210
				0.6	0.916710

Table 4: Comparison of the current study with the existing studies in the literature

	Khan et al. [3]	Kumar et al. [10]	Jawad and Nisar [26]	Awais et al. [27]	Gurejala et al. [15]	Present study
Magnetic field	Studied	Studied	Studied	Studied	Studied	Studied
Non-Newtonian fluid	Studied	Not studied	Studied	Studied	Studied	Studied
Nanofluid	Not studied	Studied	Studied	Not studied	Studied	Studied
Darcy–Forchheimer	Not studied	Not studied	Not studied	Studied	Not studied	Studied
Heat source	Studied	Not studied	Studied	Studied	Studied	Studied
Cattaneo-Christov model	Studied	Not studied	Studied	Not studied	Not studied	Studied
Radiation	Not studied	Studied	Not studied	Studied	Not studied	Studied
Activation energy	Not studied	Studied	Not studied	Studied	Not studied	Studied
Biot number	Not studied	Not studied	Not studied	Not studied	Studied	Studied

## 6 Conclusions

To represent Maxwell nanofluid flow across an expanding surface, this study utilizes the Cattaneo-Christov framework in a novel manner. This investigation evaluates the Darcy-Forchheimer dissipative flow of hydromagnetic Maxwell nanofluid over an expanding surface, incorporating radiation energy transfer, convective boundaries, activation energy, Joule heating, and energy generation. The heat transfer process is analyzed using the Cattaneo-Christov heat flux framework. This also provides the uniqueness of this study. Numerical calculations are conducted using MATLAB's bvp4c solver to analyze the flow and thermal characteristics under these conditions. The following are the analysis's key findings:

- · The thermal Grashof number and solute Grashof number serve to increase the Maxwell nanofluid velocity over an expanding surface.
- · The greater suction parameter exhibits diminishing patterns in both fluid velocity and fluid temperature profiles.
- · Higher thermal Biot parameter values lead to increased fluid temperature, while larger values of factor for temperature relaxation decrease the liquid thermal field.
- The concentration distribution drops as a consequence of development in the Brownian movement and Schmidt
- Increased Brinkman number and diffusion parameter strengthen the entropy generation.
- The coefficient of friction falls with respect to the rise in the parameter for the magnetic field, Darcy-Forchheimer parameter, and Maxwell fluid parameter.
- Higher Biot number values lead to more convective heat transport, which increases the Nusselt number overall. Conversely, as the magnetic and radiation parameters increase, the Nusselt number falls.

The results provide useful information for improving heat management in engineering systems, including MHD

devices, energy converters, and cooling technologies. Designers may maximize heat transfer, reduce friction, and regulate entropy formation by adjusting parameters such as the Biot number, magnetic field, and Brownian motion. These properties are advantageous for utilization in nanofluid-based thermal exchangers, electronics cooling, polymer processing, and biomedical flows. The future scope will involve adding changing fluid characteristics and various nanoparticle forms, as well as expanding it to unstable, three-dimensional, or rotating flows. Combining machine learning and optimization approaches can improve design processes and support implementation in advanced industrial, healthcare, and energy systems.

**Acknowledgments:** The authors extend their appreciation to the support received from Princess Nourah bint Abdulrahman University Researchers Supporting Project number (PNURSP2025R238), Princess Nourah bint Abdulrahman University, Riyadh, Saudi Arabia. This work was also supported by the Universiti Teknikal Malaysia, Melaka.

Funding information: This research work received funding from the Princess Nourah bint Abdulrahman University Researchers Supporting Project number (PNURSP2025R238), Princess Nourah bint Abdulrahman University, Riyadh, Saudi Arabia.

**Author contributions:** M.V.R. and K.M.: conceptualization, methodology, software, formal analysis, validation, writing - original draft. M.A. and F.A.: writing - original draft, data curation, investigation, visualization, validation. U.K.: conceptualization, writing - original draft, writing - review and editing, supervision, resources. J.M.N.: validation, investigation, writing - review and editing, formal analysis, project administration, funding acquisition. D.H.E. and N.S.K.: validation, writing - review and editing, software, conceptualization, provided significant feedback,

and assisted in the revised version of the manuscript. Furthermore, the authors also supported in revising the manuscript critically for important intellectual content.

**Conflict of interest:** Authors state no conflict of interest.

**Ethical approval:** Not applicable.

**Informed consent:** Not applicable.

**Data availability statement:** Data are available upon request to the author.

## References

- [1] Sara, I., W. Abdelsalam, W. Abbas, A. M. Megahed, A. Ahmed, and M. Said. A comparative study on the rheological properties of upper convected Maxwell fluid along a permeable stretched sheet. *Heliyon*, Vol. 9, 2023, id. e22740.
- [2] Amna, F. Aljuaydi, Z. Khan, and S. Islam. Numerical investigations of ion slip and hall effects on Cattaneo-Christov heat and mass fluxes in darcy-forchheimer flow of Casson fluid within a porous medium, utilizing non-fourier double diffusion theories through artificial neural networks ANNs. *International Journal of Thermofluids*, Vol. 20, 2023, id. 100475.
- [3] Khan, A., I. A. Shah, A. Khan, I. Khan, and W. A. Khan. Numerical investigation of MHD Cattaneo–Christov thermal flux frame work for Maxwell fluid flow over a steady extending surface with thermal generation in a porous medium. *International Journal of Thermofluids*, Vol. 20, 2023, id. 100418.
- [4] Jawad, M., M. K. Hameed, K. S. Nisar, and A. H. Majeed. Darcy-Forchheimer flow of maxwell nanofluid flow over a porous stretching sheet with Arrhenius activation energy and nield boundary conditions. Case Studies in Thermal Engineering, Vol. 50, 2024. id. 102830.
- [5] Iranian, D., K. Sudarmozhi, A. Chandulal, S. Al-Otaibi, A. Seethalakshmy, I. Khan, et al. Heat transfer enrichment in magnetohydrodynamic cylindrical flow of Maxwell fluid with thermal radiation and Stefan blowing effects. *Case Studies in Thermal Engineering*, Vol. 52, 2023, id. 103529.
- [6] Reddy, M. V. K. and P. Lakshminarayana. Cross-diffusion and heat source effects on a three-dimensional MHD flow of Maxwell nanofluid over a stretching surface with chemical reaction. *European Physical Journal: Special Topics*, Vol. 230, 2021, pp. 1371–1379.
- [7] Reddy, M. V. K., K. Vajravelu, P. Lakshminarayana, and G. Sucharitha. Heat source and Joule heating effects on convective MHD stagnation point flow of bi-viscous Bingham nanofluid through a porous medium with chemical reaction. *Numerical Heat Transfer, Part B: Fundamentals*, Vol. 85, 2023, pp. 286–304.
- [8] Waseem, M., M. Jawad, S. Naeem, G. Bognár, T. Alballa, H. A. E. W. Khalifa, et al. Regression analysis of Cattaneo-Christov heat and thermal radiation on 3D Darcy flow of Non-Newtonian fluids

- induced by stretchable sheet. *Case Studies in Thermal Engineering*, Vol. 61, 2024, id. 104959.
- [9] Buongiorno, J. Convective transport in nanofluids. *Journal of Heat Transfer*, Vol. 128, No. 3, 2006, pp. 240–250.
- [10] Kumar, B., Prachi, A. Singhal, R. Nandkeolyar, P. Kumar, and A. J. Chamkha. Regression analysis and features of negative activation energy for MHD nanofluid flow model: A comparative study. *Propulsion and Power Research*, Vol. 12, No. 2, 2023, pp. 273–283.
- [11] Mahabaleshwar, U. S., A. B. Vishalakshi, G. V. Bognar, and S. M. Mallikarjunaiah. Effect of thermal radiation on the flow of a Boussinesq couple stress nanofluid over a porous nonlinear stretching sheet. *International Journal of Applied and Computational Mathematics*, Vol. 8, No. 4, 2022, id. 169.
- [12] Saidulu, B. and K. Sreeram Reddy. Evaluation of combined heat and mass transfer in hydromagnetic micropolar flow along a stretching sheet when viscous dissipation and chemical reaction is present. *Partial Differential Equations in Applied Mathematics*, Vol. 7, 2023, id. 100467.
- [13] Saleem, S., B. Ahmad, A. Naseem, M. B. Riaz, and T. Abbas. Mono and hybrid nanofluid analysis over shrinking surface with thermal radiation: A numerical approach. *Case Studies in Thermal Engineering*, Vol. 54, 2024, id. 104023.
- [14] Salahuddin, T., G. Fatima, M. Awais, and M. Khan. Investigating the stagnation point and Darcy-Forchheimer flow of heat and mass transport with thermal radiation and activation energy. *Results in Engineering*, Vol. 20, 2023, id. 101534.
- [15] Gurejala, J. R., P. Manideep, S. P. Raja, and R. R. Srinivasa. Impact of viscous dissipation on MHD flow of Maxwell nanofluid across a linear stretching sheet. *International Journal of Thermofuids*, Vol. 24, 2024, id. 100832.
- [16] Mahabaleshwar, U. S., T. Maranna, L. M. Perez, G. V. Bognar, and H. F. Oztop. An impact of radiation on laminar flow of dusty ternary nanofluid over porous stretching/shrinking sheet with mass transpiration. *Results in Engineering*, Vol. 18, 2023, id. 101227.
- [17] Ahmed, F., S. K. Reza-E-Rabbi, Y. Ali Md, L. E. Ali, A. Islam, A. Rahman Md, et al. Numerical modeling of a MHD non-linear radiative Maxwell nano fluid with activation energy. *Heliyon*, Vol. 10, 2024, id. e24098.
- [18] Bafe, E. E., M. D. Firdi, and L. G. Enyadene. Magnetohydrodynamic thermo-bioconvective flow of 3D rotating Williamson nanofluid with Arrhenius activation energy in a Darcy–Forchheimer medium over an exponentially stretching Surface. *International Journal of Thermofluids*, Vol. 21, 2024, id. 100585.
- [19] Ali, L., B. Z. Ullah, M. Boujelbene, R. Apsari, S. Alshammari, I. A. Chaudhry, et al. Wave oscillations in thermal boundary layer of Darcy-Forchheimer nanofluid flow along buoyancy-driven porous plate under solar radiation region. *Case Studies in Thermal Engineering*, Vol. 54, 2024, id. 103980.
- [20] Jawad, M., A. H. Majeed, K. S. Nisar, M. B. B. Hamida, A. Alasiri, A. M. Hassan, et al. Numerical simulation of chemically reacting Darcy-Forchheimer flow of Buongiorno Maxwell fluid with Arrhenius energy in the appearance of nanoparticles. *Case Studies in Thermal Engineering*, Vol. 50, 2023, id. 103413.
- [21] Zafar, S. S., U. Khan, F. Ali, S. M. Eldin, A. M. Saeed, A. Zaib, et al. Irreversibility analysis of radiative flow of Prandtl nanofluid over a stretched surface in Darcy-Forchheimer medium with activation energy and chemical reaction. *Heliyon*, Vol. 9, 2023, id. e14877.
- [22] Li, Y., K. Ali, S. Ahmad, S. Ahmad, W. Jamshed, A. Abd-Elmonem, et al. Micro-structured fluid within a channel under static and oscillatory pressure gradients: A novel Darcy-Forchheimer flow

- investigation. Engineering Science and Technology, an International Journal, Vol. 47, 2023, id. 101544.
- [23] Ghazwani, H. A., M. Ijaz, S. Nadeemb, H. Khan, J. J. Alzabut, and A. M. Hassan. Darcy-Forchheimer flow with viscoelastic Cattaneo-Christov heat flux model and nonlinear thermal radiation: A numerical investigation. Case Studies in Thermal Engineering, Vol. 54, 2024, id. 103908.
- [24] Yasir, M., M. Khan, A. Anjum, and M. M. M. Igbal Ch. Significance of improved heat conduction on unsteady axisymmetric flow of Maxwell fluid with cubic autocatalysis chemical reaction. Heliyon, Vol. 9, 2023, id. e19004.
- [25] Jabeen, I., S. Ahmad, A. Anjum, and M. Farooq. Analysis of variable mass diffusivity in Maxwell's fluid with Cattaneo-Christov and nonlinear. Helivon, Vol. 8, 2022, id. e11850.
- [26] Jawad, M. and K. S. Nisar. Upper-convected flow of Maxwell fluid near stagnation point through porous surface using Cattaneo-Christov heat flux model. Case Studies in Thermal Engineering, Vol. 48, 2023, id. 103155.
- [27] Awais, M., T. Salahuddin, and S. Muhammad. Effects of viscous dissipation and activation energy for the MHD Eyring-powell fluid

- flow with Darcy-Forchheimer and variable fluid properties. Ain Shams Engineering Journal, 2024, id. 15102422.
- [28] Khan, M. I., S. Afzal, T. Hayat, M. Waqas, and A. Alsaedi. Activation energy for the Carreau-Yasuda nanomaterial flow: Analysis of the entropy generation over a porous medium. Journal of Molecular Liquids, Vol. 297, 2020,
- [29] Hamid, A. and M. Khan. Impacts of binary chemical reaction with activation energy on unsteady flow of magneto-Williamson nanofluid. Journal of Molecular Liquids, Vol. 262, 2018,
- [30] Zeeshan, A., O. U. Mehmood, F. Mabood, and F. Alzahrani. Numerical analysis of hydromagnetic transport of Casson nanofluid over permeable linearly stretched cylinder with Arrhenius activation energy. International Communications in Heat and Mass Transfer, Vol. 130, 2022, id. 105736.
- [31] Sharma, B. K., A. Kumar, R. Gandhi, M. M. Bhatti, and N. K. Mishra. Entropy generation and thermal radiation analysis of EMHD Jeffrey nanofluid flow: Applications in solar energy. Nanomaterials, Vol. 13, No. 3, 2023, id. 544.